






Interfacial activity dynamics of confined active droplets

Prashanth Ramesh ^{1,2} Babak Vajdi Hokmabad ^{1,3} Arnold J. T. M. Mathijssen ⁴ Dmitri O. Pushkin ⁵ and Corinna C. Maass ^{1,2,*}

¹*Max Planck Institute for Dynamics and Self-Organization,
Am Faßberg 17, 37077 Göttingen, Germany*

²*Physics of Fluids Group, Max Planck Center for Complex
Fluid Dynamics, and J.M. Burgers Center for Fluid Dynamics,
University of Twente, PO Box 217, 7500AE Enschede, Netherlands*

³*Dpt. of Chemical and Biological Engineering,
Princeton University, Princeton, NJ 08544, USA*

⁴*Dpt. of Physics & Astronomy, University of Pennsylvania,
209 S 33rd St., Philadelphia, PA 19104, USA*

⁵*Mathematics Department, University of York, Heslington, York, YO10 5DD, UK*

(Dated: November 28, 2022)

Abstract

Active emulsions can spontaneously form self-propelled droplets or phoretic micropumps. It has been predicted that the interaction with their self-generated chemical fields can lead to multistable higher-order flows and chemodynamic phenomena. However, it remains unclear how such reaction-advection-diffusion instabilities can emerge from the interplay between chemical reactions and interfacial hydrodynamics. Here, we simultaneously measure the flow fields and the chemical concentration fields using dual-channel microscopy for oil droplets that dynamically solubilize in a supramicellar aqueous surfactant solution. We developed an experimentally tractable setup with micropumps, droplets that are pinned between the top and bottom surfaces of a microfluidic reservoir, which we compare directly to predictions from a Brinkman squirmer model to account for the confinement. With increasing droplet radius, we observe (i) a migration of vortex flows from the posterior to the anterior of the droplet, analogous to a transition from pusher- to puller-type swimmers, (ii) a bistability between dipolar and quadrupolar flow modes, and, eventually, (iii) a transition to multipolar modes. We also investigate how the dynamics evolve over long time periods. Together, our observations suggest that a local build-up of chemical products leads to a saturation of the surface, which controls the propulsion mechanism. These multistable dynamics can be explained by the competing time scales of slow micellar diffusion governing the chemical buildup and faster molecular diffusion powering the underlying transport mechanism. Our results are directly relevant to phoretic micropumps, but also shed light on the interfacial activity dynamics of self-propelled droplets and other active emulsion systems.

I. INTRODUCTION

Phoretic mechanisms are widely used to actuate transport, be it externally mediated, e.g. by chemo- or electrophoresis, or self-generated: At macroscopic scales, phoresis can drive living organisms and culinary Marangoni cocktails [1], and in microfluidic environments it can power self-propelled microswimmers like active colloids or droplets [2–8], or self-driven micropumps for nutrient or fuel mixing and advection in artificial and biological systems [9–11]. In self-actuated systems, fluid transport is induced through non-equilibrium processes

* c.c.maass@utwente.nl

at the interface between the particle and the surrounding fluid where a slip velocity and/or tangential stresses are generated [12]. Various phoretic mechanisms have been reported based on the type of interactions between the particle and the ambient fluid. Regardless of the type of activity, all mechanisms rely on the inhomogeneity of a surrounding field such as gradients in solute concentration [13], temperature [14], and electric fields [15].

In the specific case of a self-driven chemically active particle or droplet, the net motion is achieved by converting chemical free energy released by the agent into mechanical work through two distinct mechanisms: the diffusiophoretic effect, introducing a finite slip velocity at the agent interface, and the Marangoni effect creating interfacial tangential stresses. In this context, we define *activity* as the conversion of undirected, chemical kinetics into mesoscopic advective flow, either driving pumping motion or a translation of the particle itself.

Reactivity gradients can be implemented by design, i.e. a built-in asymmetry, for instance by variation of the coating thickness for Janus particles [16, 17], in binary systems of interacting particle pairs [18, 19], or in droplets with adsorbed colloidal caps [20].

However, starting from a spherically isotropic particle, the only viable route to generate an interfacial reactivity gradient is by interaction with the chemical products. Chemically active droplets are one of the prime model systems studied in this context. Here, an advection-diffusion instability in the chemical field around the droplet interface causes interfacial flow modes, ranging, with increasing Péclet number Pe , from an inactive isotropic base state over a dipolar state that is propulsive in non-pinned droplets, to higher order extensile modes [21].

This emergence of higher interfacial modes and increasingly complex mesoscopic droplet motion with increasing Pe has been found to be quite general in experiments, irrespective of whether Pe is varied by way of chemical activity, droplet size or viscosity [22–25].

It was shown in [21] and subsequent works that the most general prerequisite to set this advection-diffusion activity into motion is simply the consumption of a single chemical species at a constant rate at the interface. However, experimental realisations typically require more complicated chemical pathways. A popular model system consists of oil-in-water (alternatively, water-in-oil) emulsions in which the outer phase contains fuel supplied by a surfactant at supramicellar concentrations [2, 3, 22, 23, 26]. Here, the oil phase continuously solubilizes by migrating from the bulk droplet into empty or partially saturated surfactant

micelles, leading to an interfacial Marangoni gradient that powers a self-supporting active interface (Fig. 1a).

Surfactant micelles and monomers constitute distinct species that diffuse at significantly different timescales, and these complex kinetics have been found to affect the details of the observed dynamics.

Experimental examples include the emergence of bimodal motility through micellar accumulation at hydrodynamic stagnation points [25], or trail avoidance stemming from chemotactic repulsion by long-lived chemical traces of other droplets [22, 27–31]. Current analytical and numerical work is looking beyond the one-species approximation, e.g. considering inhibitory effects of oil-filled micelles [32], necessitating coupled advection-diffusion equations for species (large micelles vs. monomers) with different individual diffusion timescales and Pe . At the current state of the art, such studies are somewhat hampered by best guesses at currently unknown molecular dynamics like aggregation kinetics, as well as computational constraints, that e.g. limit micellar aggregation numbers below typical values from experimental literature. Thus, while we see intriguing predictions, e.g. regarding multi-stable states (coexisting different vortex patterns), there is no one-to-one comparison between theory and experiment yet.

We therefore require well-controlled experimental paradigms to suggest testable geometries and provide realistic feedback to the assumptions of theory,

We propose such a system in the present study on pinned droplets, or micropumps. Here, one does not have to account for the displacements caused by the often chaotic mesoscopic motion of a motile system. Specifically, pinning gives access to steady state experimental conditions that allow for precise, simultaneous measurements of hydrodynamic and chemical fields.

In the experiments presented below, we measure the flow and chemical fields generated by pinned active droplets, and fit the vortex structure in the bulk medium to an analytical model of flow in a Brinkman medium, which allows for a qualitative analysis of the interfacial modes. We explore Pe space via changing the droplet radius, analyse steady state and long-term time dependent flow patterns around these pinned droplets with respect to anterior/posterior symmetry and multistable states and posit hypotheses on how these patterns are shaped by the multispecies chemodynamics of the droplet solubilisation.

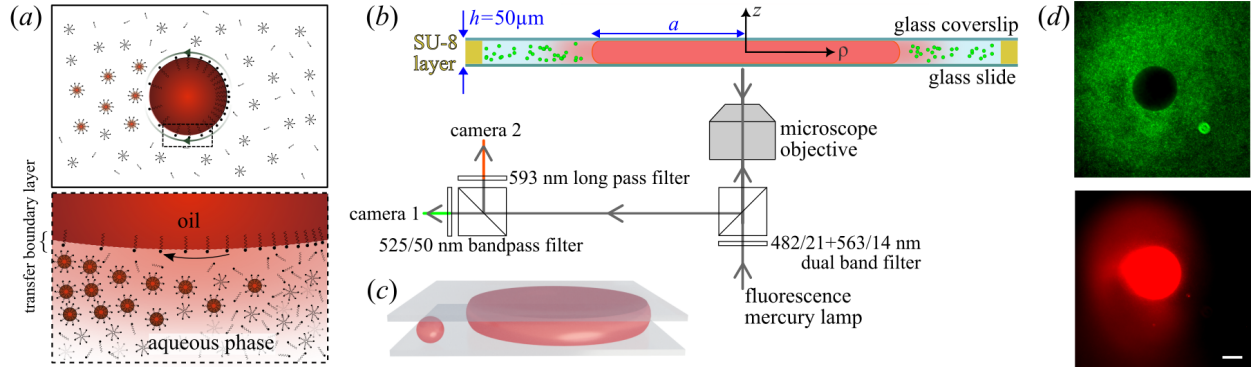


FIG. 1. (a) Schematic of droplet propulsion mechanism and a zoomed in region around the droplet interface showing surfactant monomers, empty micelles and oil-filled micelles. (b) Schematic of the dual-channel microscopy setup simultaneously visualising flow fields (camera 1) using fluorescent tracers and filled micelle concentration (camera 2) using Nile Red dye in the oil droplet. (c) Illustration of a small, spherical self-propelling droplet vs. a larger droplet pinned by squeezing between the glass top and bottom of the cell. (d) Emission from fluorescent tracers (top) and Nile Red (bottom). Scale bar: $50\ \mu\text{m}$.

II. METHODS

A. Materials and experimental protocol

Our experimental system consists of (S)-4-Cyano-4'-(2-methylbutyl)biphenyl (CB15, Synthon Chemicals) oil droplets immersed in an aqueous solution of the cationic surfactant tetradecyltrimethylammonium bromide (TTAB, Sigma-Aldrich). We note that while we have used the nematogen 5CB in some of our previous studies [33, 34], here we are using its branched isomer CB15 (or 5*CB) which is, while being a widely used chiral dopant, isotropic in its pure form at room temperature [35]. CB15 droplets of different sizes were obtained by shaking. The TTAB surfactant concentration was fixed at 5wt.% (CMC = 0.13 wt.%). Our experimental reservoir consisted of a SU-8 photoresist spacer layer spin coated on glass, framing a rectangular cell of area $13 \times 8\ \text{mm}^2$ and height of $50\ \mu\text{m}$ fabricated via UV photolithography. We filled the cell with a dilute droplet emulsion and sealed it with a glass cover slip. In our analysis we included droplets with typical radii larger than $50\ \mu\text{m}$, which were compressed into flat disks of radius $a \gtrsim 60\ \mu\text{m}$. These disks were pinned at the top and bottom of the reservoir and exhibited only pumping motion. This pinning is only effective

at relatively low surfactant concentration (here, 5wt%) – and might either be caused by oil/water/glass contact line pinning, or by short range no-slip interactions in a boundary layer of surfactant and water molecules between oil and the oleophobic glass surface. The droplet shape we observed is a flat cylinder with a convex oil-water interface, as sketched in Fig 1c.

B. Double-channel fluorescent microscopy

To simultaneously image chemical and hydrodynamic fields, we have adapted an Olympus IX-83 microscope for dual-channel fluorescent microscopy, as shown in the light path schematic in Fig. 1b. The fluorophores were excited using a fluorescence mercury lamp which is passed through a dual band excitation filter 482/21+563/14 nm. The oil phase was doped with the co-moving Nile Red (Sigma-Aldrich) dye to label oil-filled filled micelles, with an emission peak of 630 nm. The tracer particles (FluoSpheres, yellow-green fluorescent, 0.5 μm in diameter), visualising the fluid flow around the droplet, emit light at a maximum of ~ 510 nm. The emission was separated into two channels using a beam splitter and appropriate filters for each emission maximum, and recorded by two 4MP cameras (FLIR Grasshopper 3, GS3-U3-41C6M-C), at 24 fps for the green (tracers) and the red channel (dye) for short time measurements. Figure 1d shows emission from fluorescent tracers (top) and Nile red (bottom). For long time measurements, we recorded the slowly changing chemical field continuously at a reduced frame rate of 4 fps. To record tracer colloids, a higher frame rate of 24 fps was required. Due to data storage limitations, we did not record continuously for the entire experiment, but recorded 5 s sequences at 30 s intervals. Using 10X and 20X objectives focused on the cell mid-plane, the region of observation spanned $1113 \mu\text{m}^2$ and $557 \mu\text{m}^2$, with a focal depth of $3.06 \mu\text{m}$ and $1.10 \mu\text{m}$, respectively. We therefore assume all extracted flow data to represent the mid-plane values in x, y to good accuracy.

C. Image processing and data analysis

We extracted the droplet position and radius a in ImageJ using the time averaged signal from the colloidal tracer channel, where the pinned droplet appears as a dark area, A . We estimate the errors in extracted contour roundness and radius, $\Delta a/a$ to be $< 1\%$.

We extracted the flow field around the droplet by particle image velocimetry (PIV) of the tracer particles using the MATLAB-based PIVlab interface [36], with the droplet area A used as a mask. For the PIV analysis, we chose a 48×48 pixel interrogation window with 67% overlap, at a spatial resolution of $0.28 \mu\text{m}/\text{px}$. We then fit the 2D flow data generated by this procedure to the a hydrodynamic model described below in Sec. IID within the microscope’s field of view, using a least-squares fit algorithm. As PIV is unreliable near boundaries, we exclude an expanded area around the droplet, using $\rho > 1.1a$.

For further analysis we required time dependent chemical and tangential flow fields around the droplet perimeter $a\theta$ with the polar angle θ taken counter-clockwise from the droplet anterior (see dashed circles in Figure 5a,b). The flow data was taken from PIV as close to the droplet as possible, i.e. at $\rho = 1.1a$. For the chemical field, we used the channel recording the Nile red fluorescence and extracted the intensity from an annular region around A . Since the chemical signal was oversaturated around A due to the high concentration of dye in the droplet itself, we collected fluorescence data at a distance from the interface being $\rho = 1.22a$. We separately investigated the effects of varying the droplet size on the short time steady state flow (section III A), as well as time-dependent saturation effects over long-time measurements on the order of 20 min (section III D). During these long-time measurements the droplet radius reduced by approximately 7% due to solubilisation. We made sure to only include data from the first 1–2 min of experiments in the investigation of size effects shown in section III A.

D. Theory: Brinkman squirmer in 2D

To model the flow in the aqueous phase, we consider a cylindrical squirmer of radius a at low Reynolds number confined between two parallel plates separated by height h . Because confinement strongly affects the flows generated by microswimmers [37–39], we follow the framework given by [40] to calculate the flow field $\mathbf{u}(x, y)$ in the mid plane between the plates. Specifically, we approximate the 3D Stokes equations by the 2D Brinkman equations [41–44]:

$$\nabla p = \mu(\nabla^2 - k)\mathbf{u}, \quad \nabla \cdot \mathbf{u} = 0, \quad (1)$$

Here the permeability is defined as $k = 12/h^2 = 1/\lambda^2$, in direct analogy with Darcy’s law [45], and λ is the slip length.

For a pinned droplet, the oil-water interface corresponds to a circle around the coordinate origin with radius $\rho = a$ in polar coordinates (ρ, θ) . We assume that this interface is impermeable and that the flow field is determined by the tangential velocity, here given by a harmonic expansion using the Bessel functions of the second kind K_n :

$$u_\rho^n(\rho = a) = 0 \quad \text{and} \quad u_\theta^n(\rho = a) = -\frac{a}{\lambda} \frac{K_{n-1}(a/\lambda)}{K_n(a/\lambda)} b_n \sin(n\theta). \quad (2)$$

The flow field \mathbf{u} in the 2D domain around the droplet, corresponding, in the Hele-Shaw cell, to the z averaged flow in (x, y) , is then given by the pumping solution:

$$u_\rho^n = b_n \left[n \left(\frac{a}{\rho} \right)^{n+1} - n \frac{a}{\rho} \frac{K_n(\rho/\lambda)}{K_n(a/\lambda)} \right] \cos(n\theta) \quad (3)$$

$$u_\theta^n = b_n \left[n \left(\frac{a}{\rho} \right)^{n+1} + \frac{a}{\lambda} \frac{K'_n(\rho/\lambda)}{K_n(a/\lambda)} \right] \sin(n\theta) \quad (4)$$

The flow patterns around the droplet are characterised by the first two coefficients b_1, b_2 : First, their weights determine the dominant flow mode, which is dipolar for $|b_2/b_1| < 1$ and quadrupolar for $|b_2/b_1| > 1$ [40, 46]. For illustration, the supplementary figure S8 shows the calculated stream lines for increasing $|b_2/b_1|$ in the Brinkman model. Second, for a primarily dipolar flow pattern, the sign of b_2 determines the location of the dominant vortex pair: $b_2 > 0$ results in an anterior and $b_2 < 0$ a posterior location, with the droplet anterior defined at $\theta = 0$. In our fits of the experimental velocity field to this model, we use b_1, b_2 as fit parameters with $b_n = 0$ for $n > 2$, and, figure 6 excepted, all xy data plots have been rotated to have the droplet's anterior or $\theta = 0$ axis to point to the right, in positive x .

We note that, using the Brinkman description, we assume that $u(z) \approx 0$: all monopolar flow modes like a gravitational force monopole (cf. [24, 47] for sedimenting droplets) should be suppressed by the strong z confinement of the Hele-Shaw geometry.

III. RESULTS

For droplets driven by micellar solubilisation, self-sustaining propulsive or pumping flows develop when the Péclet number Pe exceeds a critical threshold [21]. Pe is given by the ratio of advective to diffusive transport of surfactant monomers from the droplet interface to oil-filling micelles [3], and can be estimated in the single-species picture as follows (cf.

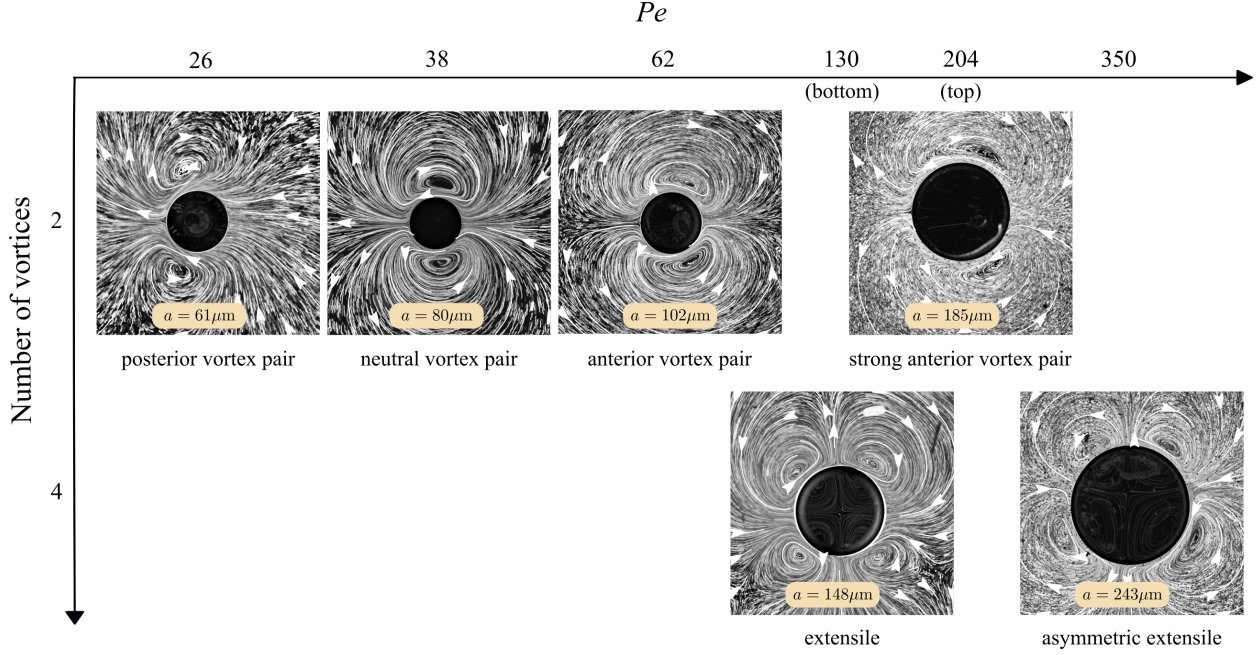


FIG. 2. Streak visualisation [48] of flow fields generated by pumping active droplets for increasing droplet radius a , with superimposed streamlines from PIV analysis. We observe a shift of the vortex pair from the droplet posterior to the anterior in the top row, corresponding to $a = 61 \mu\text{m}$, $a = 80 \mu\text{m}$, and $a = 102 \mu\text{m}$, and on further increase of a , a bistable regime between a dipolar ($a = 185 \mu\text{m}$) and a quadrupolar flow mode ($a = 148 \mu\text{m}$). For larger radii, we only see the quadrupolar mode ($a = 243 \mu\text{m}$). See also videos S1 and S2.

eqn. 1 and appendix B.2 in [25], following [2, 12, 49]):

$$Pe \approx \frac{18\pi^2}{k_B T} q_s r_s^2 \zeta a^2 \mu^i \left[\mu \left(\frac{2\mu + 3\zeta/a}{2\mu + 3} \right) \right] \quad (5)$$

Here, a is the droplet radius, $\mu = \mu^o/\mu^i$ the viscosity ratio between outer and inner medium, $\zeta \sim 10 \text{ nm}$ the characteristic length scale over which surfactant monomers interact with the droplet, $r_s \sim 10 \times 10^{-10} \text{ m}$ the length of a monomer, and $q_s = D\mathbf{n} \cdot \nabla c$ is the isotropic interfacial surfactant desorption rate per area.

We use this definition of Pe for the present geometry as well, since the underlying chemical processes are identical: an increase in the droplet radius a corresponds to an increase of Pe .

A. Flow field characterisation and comparison with the Brinkman squirmer model

We begin with a classification of the observed flow patterns around pumping flat droplets, as shown in figure 2, and the supporting videos S1 and S2. For small radii, $a = 61 \mu\text{m}$, or $Pe = 26$, we find one posterior droplet pair. With increasing droplet radius, $a = 80 \mu\text{m}$ or $Pe = 38$, the vortex pair shifts towards the midline (‘neutral’ position) and finally to the droplet anterior, for $a = 102 \mu\text{m}$ with $Pe = 62$.

On further increasing the droplet radius, we observe a bistable regime, featuring either a vortex pair displaced further towards the droplet anterior ($a = 185 \mu\text{m}$, $Pe = 204$) or a symmetric extensile or quadrupolar flow field ($a = 148 \mu\text{m}$, $Pe = 130$). For even bigger droplet radii we find only the quadrupolar mode, with an increasing asymmetry in the vortex positions which shift towards the anterior ($a = 243 \mu\text{m}$, $Pe = 350$).

For a quantitative evaluation of the interfacial modes, we measure the flow fields by PIV and compare them to the Brinkman model by fitting the flow fields via b_1, b_2 as shown in figure 3 where the panels (a)–(e) analyse the data presented in figure 2. The streamlines in the top row show a good quantitative agreement between experimental data (top half) and the Brinkman model (bottom half).

The model successfully captures the vortex positions in the bulk medium, as shown by the comparison of measured and fitted streamlines in the top row; and by the small and unstructured residual flow fields in the far field (bottom row).

In analogy to the squirmer model for motile droplets [50, 51], we can define a parameter $\beta = b_2/b_1$ that indicates the vortex centre position. A posterior vortex pair corresponds to $b_2/b_1 < 0$, neutral vortices to $b_2/b_1 = 0$ and anterior vortices to $b_2/b_1 > 0$. A quadrupolar configuration is caused by a dominant second mode with $|b_2/b_1| > 1$. However, for dipolar anterior vortices (figure 3e), the fit to the Brinkman model up to second order somewhat under-predicts θ_v , which leads to distinct vortex structures in the residual field.

B. Squirmer parameter and phase diagram

Using the data obtained by fitting the Brinkman model to the experimental data, we plot the change of the squirmer parameter b_2/b_1 with the droplet radius a in figure 4a. With increasing radius, b_2/b_1 increases from negative to zero and then to positive values, but

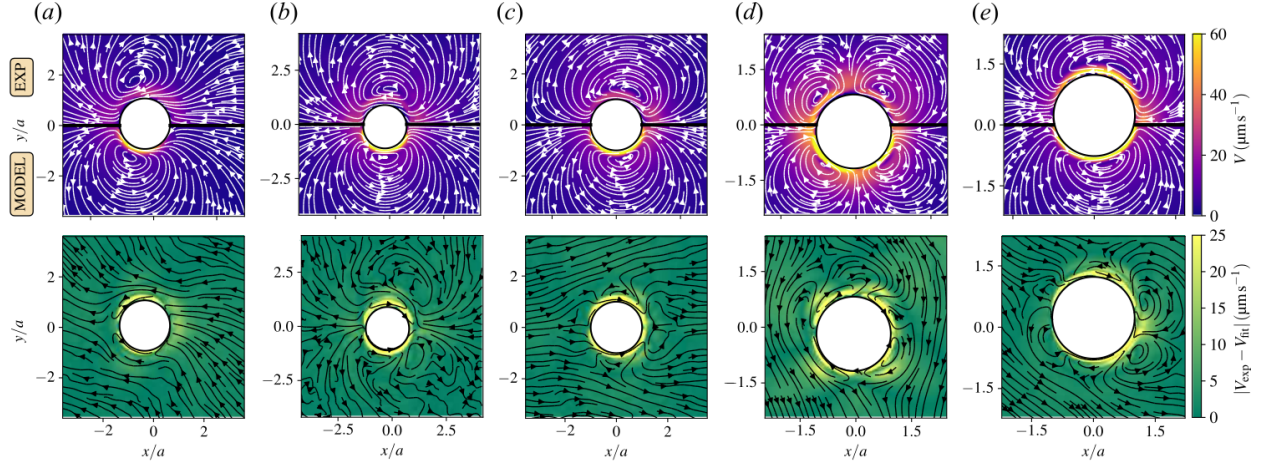


FIG. 3. Top row: Comparison between the experimental flow fields v_{exp} (top half of each panel) and the Brinkman model fits v_{fit} (bottom half) for different Pe , with fit parameters b_1, b_2 . (a) $Pe = 26$ ($b_2/b_1 = -0.529$), (b) $Pe = 38$ ($b_2/b_1 = -0.001$), (c) $Pe = 62$ ($b_2/b_1 = 0.191$), (d) $Pe = 130$ ($b_2/b_1 = 4.915$) and (e) $Pe = 204$ ($b_2/b_1 = 0.175$). Depending on the b_2/b_1 ratio, we note a shift of the vortex pair towards the droplet anterior, and a bistability of dipolar and quadrupolar patterns for large droplets. Bottom row: Residual flow fields, $— |v_{\text{exp}} - v_{\text{fit}}|$.

still remains smaller than one, which indicates a dominant first mode. This b_2/b_1 transition reflects the vortex shift from the droplet posterior to a neutral and then an anterior position. We further calculate the vortex angle θ_v , defined as the polar angle of the line between $\rho = 0$ and the location of $\mathbf{u}(x, y) = 0$ at the centre of the respective vortex (figure 4e). To compare the vortex position predictions from the Brinkman model, we plot the vortex angles obtained from both experiment and theory versus the radius in figure 4b. We observe an excellent agreement up to large radii of $a \gtrsim 150 \mu\text{m}$. Here, with a strong anterior shift, the experimental vortex centre position is underpredicted by the model.

At larger radii, we predominantly find quadrupolar flow fields, *i.e.* a dominant second mode. For classification, we plot the different modes in the space spanned by $|b_2/b_1|$ and a as shown in figure 4c. The phase diagram is divided into three regions, namely, (i) ‘vortex pair’, (ii) ‘bistable’, featuring either a strong anterior vortex pair or a symmetric extensile flow and (iii) ‘asymmetric extensile’, where the anterior vortex pairs are displaced inwards. The dashed horizontal line, $|b_2/b_1| = 1$, separates dipolar (below) and quadrupolar (above) flow fields. For large droplets, the quadrupolar state also loses fourfold symmetry, as the vortices

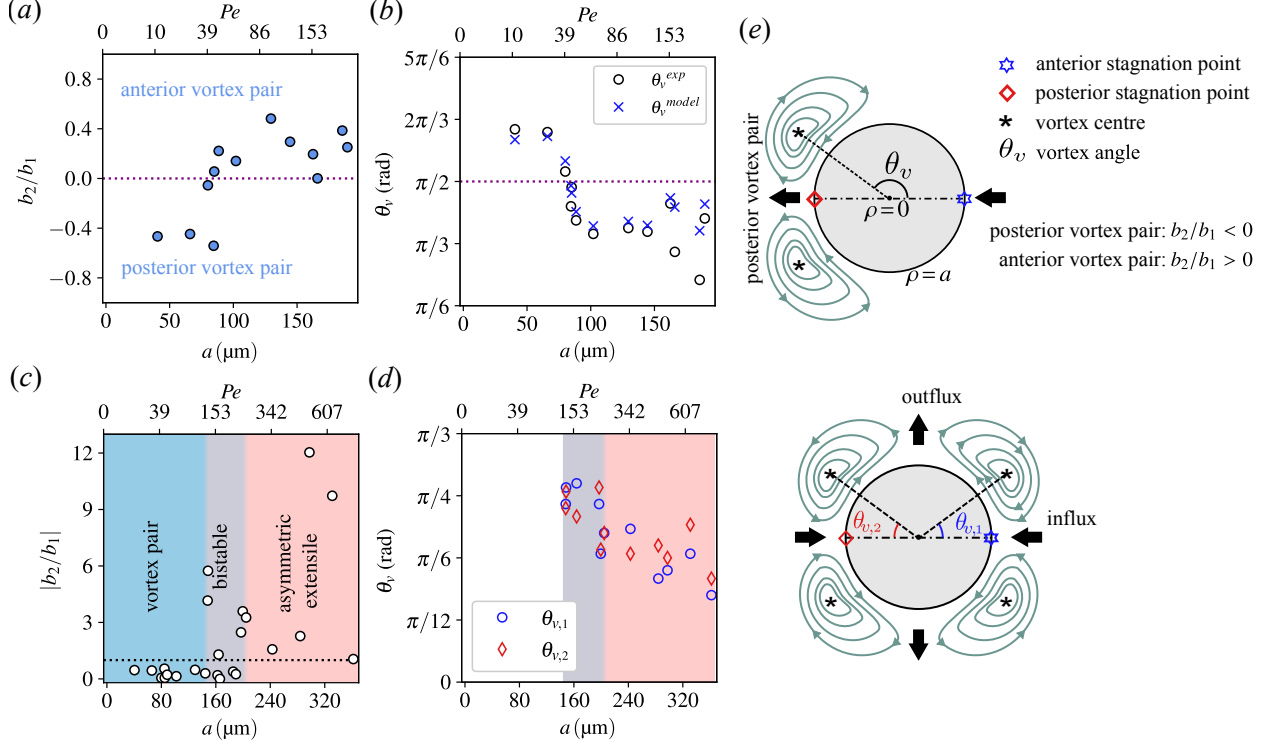


FIG. 4. (a,c) Variations of squirmer parameter b_2/b_1 versus Pe . (b,d) Variations of angle between front stagnation point and vortex centre θ_v versus Pe . (e) Schematic defining the vortex angle.

move towards the anterior and posterior stagnation points. To characterise this asymmetry, we plot the vortex angles for both anterior, $\theta_{v,1}$, and posterior, $\theta_{v,2}$, vortex pairs in figure 4d. For the symmetric quadrupolar state, the vortex angle is $\theta_v \approx \pi/4$ (grey region), whereas in the asymmetric configuration, $\theta_v < \pi/4$ (pink region). We note that for both dipolar and quadrupolar asymmetric states, the vortices are pulled towards stagnation points with radial influx.

C. Simultaneous chemical and flow field characterisation

For a deeper analysis, we simultaneously measure the droplet flow fields and the chemical concentration fields using dual channel microscopy as described above in section II B. Previous studies have shown that oil-filled micelles are considerably larger than the reactive species, *i.e.* surfactant monomers and will therefore diffuse much more slowly [25], such that we can expect them to aggregate at stagnation points and cause secondary inhibition effects as proposed in [32]. Here, oil-filled micelles are labelled by Nile red dye co-moving with the

oil phase.

In figure 5 (a-e), we set out the relation between chemical and flow field for a close to neutral dipolar droplet. Panel (a) maps the field of the tangential velocity u_θ , with superimposed streamlines, while panel (b) displays a contour plot of the Nile red emission I . We further extract the profiles u_θ and $I(\theta)$ around the droplet along the dashed lines, as displayed in panels (c) and (d), with the gradient of the intensity profile in panel (e).

If we now assume that the interfacial surfactant density is depleted in the presence of filled micelles, an extremum of the gradient in the chemical field $\partial_\theta I^{\max}$ should correlate to a Marangoni gradient in the interface and therefore to an extremum u_θ^{\max} of the tangential velocity. Furthermore, the Brinkman model solution predicts that the polar angle θ_v for the stagnation points of the vortex pairs coincides with the angle of maximum tangential flow $\theta(u_\theta^{\max})$. We have plotted the respective angles of θ_v , $\theta(u_\theta^{\max})$ and $\theta(\partial_\theta I^{\max})$ in panel (f).

As the droplet radius a increases, the vortex position shifts from the posterior at $\theta_v > \pi/2$ to the anterior at $\theta_v < \pi/2$. In good agreement with the Brinkman model, $\theta(u_\theta^{\max})$ coincides with θ_v . $\theta(\partial_\theta I^{\max})$ shows a similar shift with increasing droplet radius, but with an offset towards higher θ values compared to θ_v and $\theta(u_\theta^{\max})$. This may be due to a systematic overestimation – as noted in section II C, the fluorescence has to be measured away from the interface, where the micelles have already been advected further towards the droplet posterior.

This displacement of maximal chemical gradient location with increasing droplet radius suggests a saturation effect by oil-filled micelles that determines the vortex position θ_v , which we will discuss in detail below.

D. Long time evolution of the pumping droplet

Until now, we have looked at short-time dynamics. We will now investigate long-term dynamics, where self-interactions become more important: We expect reaction products to recirculate and interact with the droplet again after timescales longer than the advective one. This could influence the long-term interfacial activity dynamics. To quantify this, we recorded dual-channel microvideographs of flow and chemical fields around a droplet with a dipolar flow field, and analysed the long-time interfacial dynamics (see also Video S3).

Figure 6a shows, for increasing time, colloidal tracer images with selected streamlines that

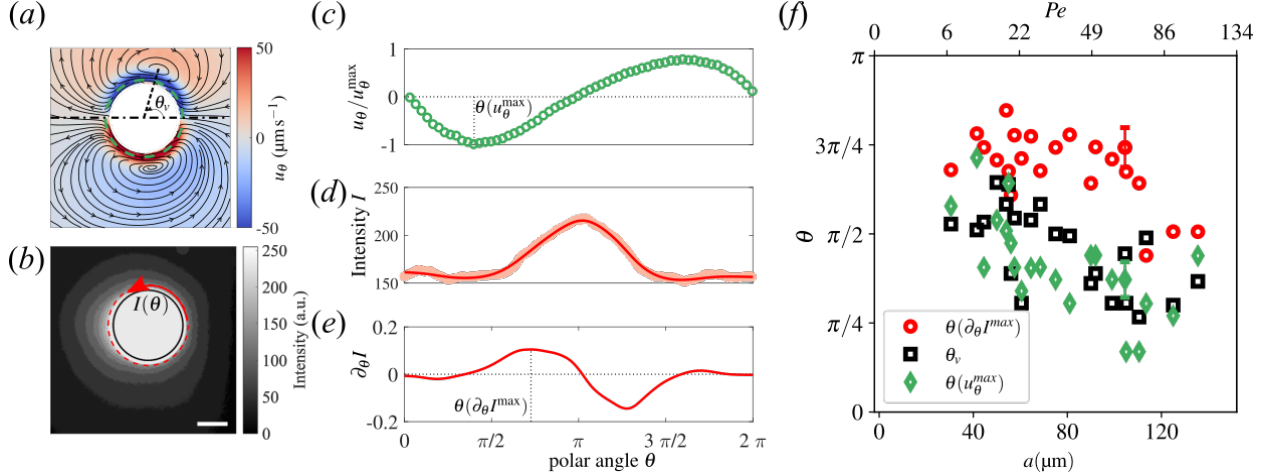


FIG. 5. (a) Flow streamlines around a pumping droplet at $Pe = 65$ colour coded by tangential velocity. Tangential velocity u_θ around the droplet interface is extracted along the green dashed circle. (b) Corresponding contour plot of fluorescent emission by Nile red doped oil droplet and filled micelles. Intensity profile around the droplet interface is extracted along the red circle. Scale bar: $50 \mu\text{m}$. (c) Tangential velocity profile at the interface. (d) Intensity profile of filled micelle concentration around the droplet. (e) corresponding gradient profile. (f) Variations of vortex angle (black), maximum tangential velocity (green) and maximum chemical gradient location around the droplet (red) versus Pe . We have added a representative error bar that quantifies the systematic error due to the measurement being away from the droplet interface. All three observables decrease with increasing Pe .

illustrate the extracted flow field. We have plotted the tangential velocity at the interface, using the diverging colour map from panel (c) below, such that green corresponds to positive (counterclockwise) and purple to negative flow, while yellow regions mark negligible flow with $|u_\theta| < 1 \mu\text{m s}^{-1}$, as expected for both the anterior and posterior stagnation points. At $t = 0$, the entire remaining droplet perimeter is active. With increasing time, as the droplet solubilises, oil-filled micelles build up and accumulate around the posterior stagnation point $\theta = \pm\pi$. In this area, the tangential flow speed decreases. The inactive region grows over time, as shown in the broadening yellow section of the tangential velocity map, while the vortices shift towards the anterior.

At long times ($t = 22$ min.), only a very small region at the droplet anterior is active and soon the entire droplet is rendered inactive.

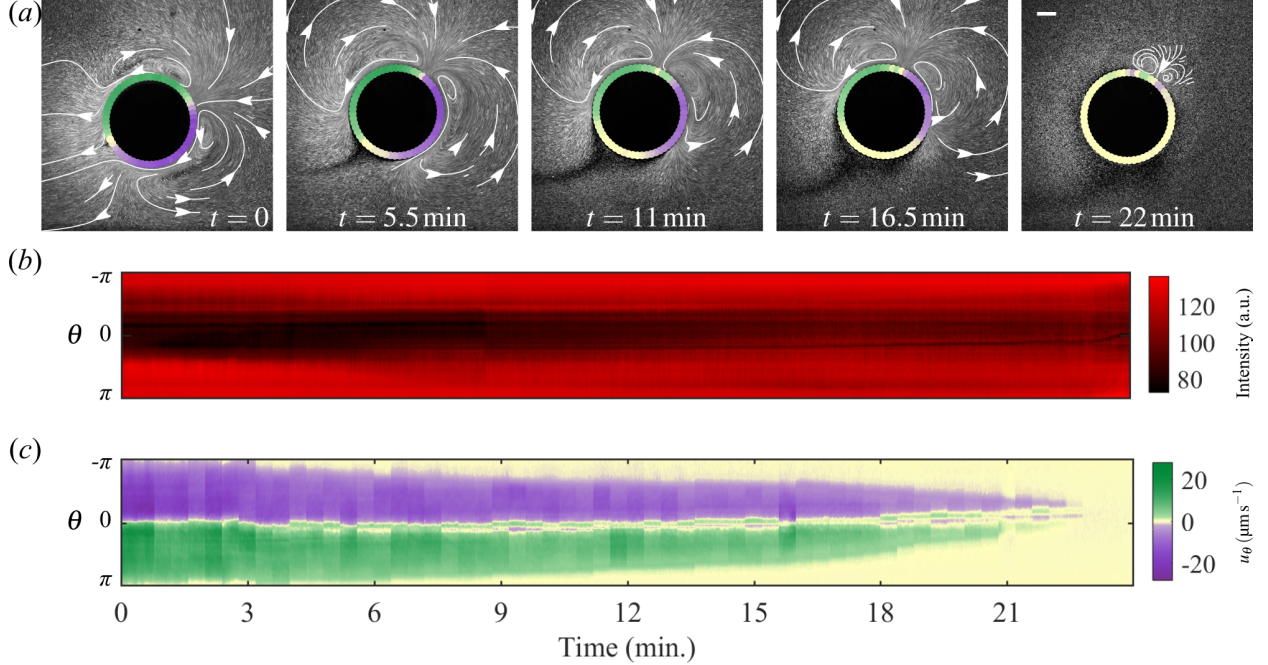


FIG. 6. (a) Time evolution of streamlines around a pumping droplet at $Pe = 241$ and $a = 201 \mu\text{m}$. As time increases, the inactive region starting from the rear stagnation point grows around the interface due to saturation by filled micelles. This leads to droplet inactivity at long time. Scale bar: $100 \mu\text{m}$. (b) Time evolution of filled micelle concentration around the droplet interface. $\theta = 0$ indicates the anterior stagnation point. (c) Time evolution of tangential velocity around the droplet interface. See also Video S3.

To track the continuous evolution of filled micelle concentration and tangential velocity at the droplet interface, we have mapped them onto kymographs in t, θ space in figure 6 (b) and (c). At $t = 0$, the red fluorescence from oil filled micelles is centred around the posterior stagnation point at $\theta = \pm\pi$; the dark region around the anterior stagnation point indicates mostly empty micelles. With increasing time, as the number of oil-filled micelles increases, the red region at the posterior broadens until it fills almost the entire droplet perimeter. This is also evident from figure 6c, where the green and purple bands of tangential flow corresponding to the two vortices narrow over time and recede towards $\theta = 0$, while the yellow region broadens, indicating inactivity with $|u_\theta| < 1 \mu\text{m/s}$. For long times, this gradual saturation renders the droplet entirely inactive. This saturation is different from what to expect in motile droplets as they can escape their own chemical exhaust [25].

E. The effect of micelle saturation

Finally, we want to discuss two observations: First, with increasing droplet size and Pe , we have seen a displacement trend from posterior to anterior for both vortex-pair location, and maximum concentration gradient location. Second, long time measurements showed a saturation effect by filled micelles which leads to similar vortex location displacement, and eventually the stopping of activity. This observation is different from numerical work on models assuming a constant interfacial activity by interaction with a single chemical species: a good example is provided in Fig. 3 of [49], where, with increasing Pe , the dipolar vortex centre changes from midline symmetry, to a pusher-type posterior location, to a quadrupolar state with front-back symmetry.

We note that these models use a spherical 3D boundary with an axisymmetric constraint and no external forces: we are not aware of studies on a Brinkman quasi-2D system model with a pinning force.

We may however speculate that the different evolution of vortex patterns is mediated by the solubilization mechanism, to which a generalised one-species model is agnostic.

Micelles will not absorb an infinite number of oil molecules (else the solubilization would create new droplets, which defies thermodynamics). Assuming, to first order, a constant flux of absorbing micelles along an active interface, and a constant rate at which they absorb oil from the boundary layer, there should be a fixed saturation time t_s , and associated length beyond which micelles will not fill any further. This length scale limits the size of the vortex patterns around the droplet.

To extract this length scale, we analyze the steady state flow fields around of droplets of different sizes (Section III A) with respect to two quantities. First, the length $a\theta_v$, which measures the arc length from the anterior stagnation point to the vortex centre. We assume $a\theta_v$ to scale with the saturation length, as θ_v marks the angle where the vortex streamlines begin to reorient away from the interface. Second, the average tangential velocity at the droplet interface $\bar{u}_\theta = \langle u_\theta(\rho = a, \theta) \rangle_{\theta=0.001}^{\theta=\theta_v}$, which is calculated using the Brinkman model fit to the PIV flow field measurements. The saturation time t_s defined above should now scale with $t_s = a\theta_v/\bar{u}_\theta$.

We have plotted the experimentally determined $a\theta_v$, \bar{u}_θ and t_s vs. a in figure 7. We find that both $a\theta_v$ and \bar{u}_θ increase with the droplet radius a and that $t_s = (0.92 \pm 0.17)$ s is

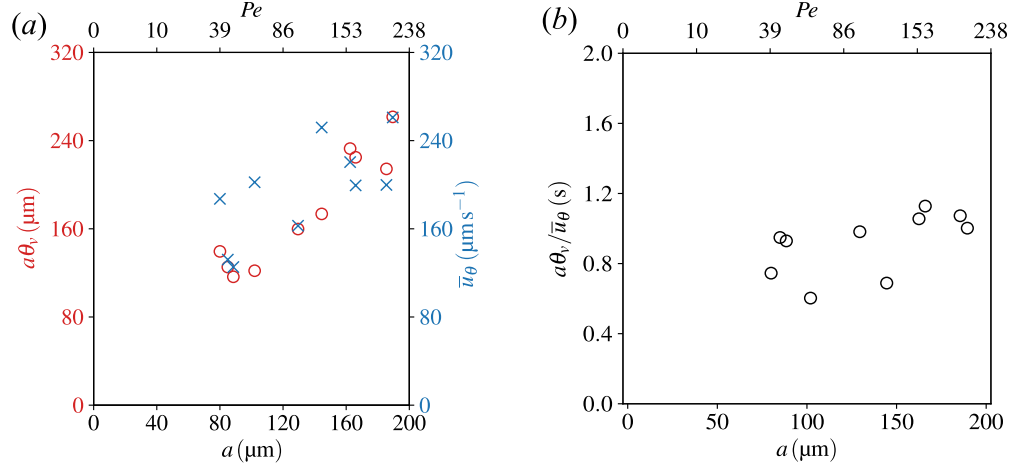


FIG. 7. (a) Vortex arc length $a\theta_v$ and averaged tangential velocity \bar{u}_θ versus droplet radius a . (b) Saturation time $a\theta_v/\bar{u}_\theta$ versus droplet radius a , as extracted from the quantities plotted in (a).

constant. This indicates that for a fixed surfactant concentration the time for the micelles to become saturated is independent from the size of the droplet, and that this time scale sets the region of interfacial activity and thereby the anterior/posterior vortex configuration. We note that this argument does not hold for small droplets where the vortices are displaced beyond the posterior stagnation point, as a needs to be sufficiently large for the micelles to saturate while they are passing the interface.

Given the above assumptions, it also follows that for long times, i.e. beyond the time scale of the steady state analysed above, the continuous recirculation of filled micelles advects fewer empty micelles at the droplet anterior, which fill up faster. This leads to a gradual decrease of the saturation times and length scales, which is what we observe in figure 6 and Video S3.

IV. DISCUSSION AND OUTLOOK

Chemically active droplets produce the flow fields that make them self-propelling microswimmers or pinned micropumps, primarily via Marangoni gradients caused by chemical reactions at the interface. In the experiments detailed above, we have studied chemical and flow fields around pinned droplets depending on both size and activity duration and performed a hydrodynamic mode analysis using a Brinkman squirmer model to account for quasi 2D confinement and a Péclet number Pe adapted to the specific chemical system.

This allows us to compare our findings to recent developments in numerical and analytical models using similar Pe based mode stability approaches.

We confirmed that the extrema in interfacial flow, and thereby the structure of the vortex field around the droplet, are correlated to gradients in the local concentration of reactivity products, which shift around the perimeter with both increasing droplet size and progressing time. We have seen multistability of dipolar and quadrupolar modes, and an overall tendency of posterior-to-anterior displacement with increasing droplet size or experimental progress, which, during the observation of a droplet for a longer time, leads eventually to an inactive droplet, where the interface is fully fouled up by chemical buildup. The analysis of our size-dependent data strongly suggests that the vortex structure is determined by the time scale of fuel conversion, as evidenced by a time independent micellar saturation time.

Our findings provide illustration to recent developments in analytical advection-diffusion models. Historically, minimal models assumed an uniform interfacial reaction rate [2, 21], which indeed yields higher order propulsive and extensile (*e.g.*, dipolar to quadrupolar) modes with increasing Pe with good semi-quantitative experimental agreement. However, open questions remain for further investigation. Notably, simulations [49] found a transition from neutral squirmer $\beta = 0$ to pusher, $\beta < 0$ with a posterior vortex pair, to quadrupolar extensile with increasing Pe , while our experiments presented above show an *increase* of β with increasing Pe , albeit in a different, non-pinned, geometry. However, in experiments on motile droplets driven by micellar solubilisation, sufficiently small swimmers are commonly weak pushers [23, 40, 47]. Pusher-to-neutral tendencies, *i.e.* an increase of β , with increasing droplet radius have also been reported for moving droplets [23], suggesting that the divergent behaviour is not a consequence of pinning. Bistability of dipolar and quadrupolar states was found numerically for both a 3D swimmer held stationary [52], as well as in a model where the interfacial reactivity was assumed to be inhibited by oil-filled micelles [32]. Interestingly, in the latter case, the region of multistability increased with the inhibition parameter. The flow field of a Brinkman squirmer with a localised interfacial gradient, corresponding to our assumption of a predominantly inactivated interface for long times, has been evaluated as well [44], yielding very similar vortex patterns. We note, however, that these calculations were based on an preimposed interfacial tension gradient (or, experimentally, localised heating), such that the underlying physical mechanism is different from the one causing our self-evolving profile.

Beyond the implications for individual motility, multistable and higher mode flow patterns matter in the collective dynamics of active matter, and in their interactions with confined geometries. [53] showed that developing starfish embryos generate different flow patterns during its development process, which determine their self-organisation (formation, dynamics, and dissolution) into living crystals. Analogously, in artificial autophoretic systems, rotational instabilities on the individual scale [23, 25] can carry through to the collective dynamics, where we have recently found Pe dependent stability and collective rotation in self-assembled planar clusters [24]. Here, the superposition of self-generated chemical fields might well provide a mechanism for the emergence of stable collective rotational states. Our analysis of interfacial activity dynamics is also directly relevant to the study of active carpets [54, 55].

Impermeable boundaries like walls will also affect the spreading of inhibitory chemical products and affect the stability of hydrodynamic modes, as recently demonstrated for a droplet near a wall [52]. Experimentally, such inhibitory effects in confinement can immobilise consecutive droplets in an active Bretherton scenario [56] or cause reorientation up to self-trapping [27, 29, 31].

Understanding and modelling such phenomena from the molecular scale upwards is a daunting task, given the manifold species one has to keep track of and that the complex multistable dynamics are likely initiated by the competing time scales of slow micellar diffusion governing the chemical buildup and faster molecular diffusion powering the underlying advection-diffusion mechanism. We therefore propose the tools and experimental geometry in this study as a well-defined and quantifiable testing case to investigate in matching theoretical modelling.

V. ACKNOWLEDGMENTS

We gratefully acknowledge fruitful discussions with Prof. Jörn Dunkel at MIT and experimental optics support by Dr. Kristian Hantke at MPI-DS. We expressly acknowledge the contribution of experimental data by Myriam Rahalia, whom we were unable to contact

at the time of submission.

- [1] A. J. T. M. Mathijssen, M. Lisicki, V. N. Prakash, and E. J. L. Mossige, Culinary fluid mechanics and other currents in food science, [arXiv](#) , [2201.12128](#) (2022).
- [2] Z. Izri, M. N. van der Linden, S. Michelin, and O. Dauchot, Self-Propulsion of Pure Water Droplets by Spontaneous Marangoni-Stress-Driven Motion, [Physical Review Letters](#) **113**, [248302](#) (2014).
- [3] S. Herminghaus, C. C. Maass, C. Krüger, S. Thutupalli, L. Goehring, and C. Bahr, Interfacial mechanisms in active emulsions, [Soft Matter](#) **10**, 7008 (2014).
- [4] C. C. Maass, C. Krüger, S. Herminghaus, and C. Bahr, Swimming Droplets, [Annual Review of Condensed Matter Physics](#) **7**, 171 (2016).
- [5] D. Babu, N. Katsonis, F. Lancia, R. Plamont, and A. Ryabchun, Motile behaviour of droplets in lipid systems, [Nature Reviews Chemistry](#) , 1 (2022).
- [6] S. Birrer, S. I. Cheon, and L. D. Zarzar, We the Droplets: A Constitutional Approach to Active and Self-Propelled Emulsions, [Current Opinion in Colloid & Interface Science](#) , 101623 (2022).
- [7] P. Dwivedi, D. Pillai, and R. Mangal, Self-Propelled Swimming Droplets, [Current Opinion in Colloid & Interface Science](#) , 101614 (2022).
- [8] S. Michelin, Self-Propulsion of Chemically Active Droplets, [Annual Review of Fluid Mechanics](#) **55**, null (2023).
- [9] T. Yu, A. G. Athanassiadis, M. N. Popescu, V. Chikkadi, A. Güth, D. P. Singh, T. Qiu, and P. Fischer, Microchannels with Self-Pumping Walls, [ACS Nano](#) **14**, 13673 (2020).
- [10] W. Gilpin, V. N. Prakash, and M. Prakash, Vortex arrays and ciliary tangles underlie the feeding–swimming trade-off in starfish larvae, [Nature Physics](#) **13**, 380 (2017).
- [11] G. C. Antunes, P. Margaretti, J. Harting, and S. Dietrich, Pumping and Mixing in Active Pores, [Physical Review Letters](#) **129**, 188003 (2022).
- [12] J. L. Anderson, Colloid transport by interfacial forces, [Annual Review of Fluid Mechanics](#) **21**, 61 (1989).
- [13] R. Golestanian, T. B. Liverpool, and A. Ajdari, Propulsion of a molecular machine by asymmetric distribution of reaction products, [Physical Review Letters](#) **94**, 220801 (2005).

- [14] N. O. Young, J. S. Goldstein, and M. J. Block, The motion of bubbles in a vertical temperature gradient, [Journal of Fluid Mechanics](#) **6**, 350 (1959).
- [15] M. Z. Bazant and T. M. Squires, Induced-Charge Electrokinetic Phenomena: Theory and Microfluidic Applications, [Physical Review Letters](#) **92**, 066101 (2004).
- [16] S. Ebbens, D. A. Gregory, G. Dunderdale, J. R. Howse, Y. Ibrahim, T. B. Liverpool, and R. Golestanian, Electrokinetic effects in catalytic platinum-insulator Janus swimmers, [EPL \(Europhysics Letters\)](#) **106**, 58003 (2014).
- [17] A. I. Campbell, S. J. Ebbens, P. Illien, and R. Golestanian, Experimental observation of flow fields around active Janus spheres, [Nature Communications](#) **10**, 1 (2019).
- [18] S. Y. Reigh and R. Kapral, Catalytic dimer nanomotors: Continuum theory and microscopic dynamics, [Soft Matter](#) **11**, 3149 (2015).
- [19] S. Y. Reigh, P. Chuphal, S. Thakur, and R. Kapral, Diffusiophoretically induced interactions between chemically active and inert particles, [Soft Matter](#) **14**, 6043 (2018).
- [20] S. Ik Cheon, L. B. Capaverde Silva, A. S. Khair, and L. D. Zarzar, Interfacially-adsorbed particles enhance the self-propulsion of oil droplets in aqueous surfactant, [Soft Matter](#) **17**, 6742 (2021).
- [21] S. Michelin, E. Lauga, and D. Bartolo, Spontaneous autophoretic motion of isotropic particles, [Physics of Fluids](#) **25**, 061701 (2013).
- [22] A. Izzet, P. G. Moerman, P. Gross, J. Groenewold, A. D. Hollingsworth, J. Bibette, and J. Brujic, Tunable Persistent Random Walk in Swimming Droplets, [Physical Review X](#) **10**, 021035 (2020).
- [23] S. Suda, T. Suda, T. Ohmura, and M. Ichikawa, Straight-to-Curvilinear Motion Transition of a Swimming Droplet Caused by the Susceptibility to Fluctuations, [Physical Review Letters](#) **127**, 088005 (2021).
- [24] B. V. Hokmabad, A. Nishide, P. Ramesh, C. Krüger, and C. C. Maass, Spontaneously rotating clusters of active droplets, [Soft Matter](#) **18**, 2731 (2022).
- [25] B. V. Hokmabad, R. Dey, M. Jalaal, D. Mohanty, M. Almukambetova, K. A. Baldwin, D. Lohse, and C. C. Maass, Emergence of Bimodal Motility in Active Droplets, [Physical Review X](#) **11**, 011043 (2021).
- [26] C. H. Meredith, P. G. Moerman, J. Groenewold, Y.-J. Chiu, W. K. Kegel, A. van Blaaderen, and L. D. Zarzar, Predator-prey interactions between droplets driven by non-reciprocal oil

- exchange, *Nature Chemistry* **12**, 1136 (2020).
- [27] C. Jin, C. Krüger, and C. C. Maass, Chemotaxis and autochemotaxis of self-propelling droplet swimmers, *Proceedings of the National Academy of Sciences* **114**, 5089 (2017).
- [28] P. G. Moerman, H. W. Moyses, E. B. van der Wee, D. G. Grier, A. van Blaaderen, W. K. Kegel, J. Groenewold, and J. Brujic, Solute-mediated interactions between active droplets, *Physical Review E* **96**, 032607 (2017).
- [29] K. Lippera, M. Benzaquen, and S. Michelin, Alignment and scattering of colliding active droplets, *Soft Matter* **17**, 365 (2020).
- [30] K. Lippera, M. Morozov, M. Benzaquen, and S. Michelin, Collisions and rebounds of chemically active droplets, *Journal of Fluid Mechanics* **886**, 10.1017/jfm.2019.1055 (2020).
- [31] B. V. Hokmabad, J. Agudo-Canalejo, S. Saha, R. Golestanian, and C. C. Maass, Chemotactic self-caging in active emulsions, *Proceedings of the National Academy of Sciences* **119**, e2122269119 (2022).
- [32] M. Morozov, Adsorption inhibition by swollen micelles may cause multistability in active droplets, *Soft Matter* **16**, 5624 (2020).
- [33] C. Krüger, G. Klös, C. Bahr, and C. C. Maass, Curling Liquid Crystal Microswimmers: A Cascade of Spontaneous Symmetry Breaking, *Physical Review Letters* **117**, 048003 (2016).
- [34] C. Krüger, C. Bahr, S. Herminghaus, and C. C. Maass, Dimensionality matters in the collective behaviour of active emulsions, *The European Physical Journal E* **39**, 64 (2016).
- [35] J. Mayer, W. Witko, M. Massalska-Arodz, G. Williams, and R. Dabrowski, Polymorphism of right handed (S) 4-(2-Methylbutyl) 4'-Cyanobiphenyl, *Phase Transitions* **69**, 199 (1999).
- [36] W. Thielicke and E. Stamhuis, PIVlab – Towards User-friendly, Affordable and Accurate Digital Particle Image Velocimetry in MATLAB, *Journal of Open Research Software* **2**, e30 (2014).
- [37] A. J. T. M. Mathijssen, A. Doostmohammadi, J. M. Yeomans, and T. N. Shendruk, Hydrodynamics of micro-swimmers in films, *Journal of Fluid Mechanics* **806**, 35 (2016).
- [38] R. Jeanneret, D. O. Pushkin, and M. Polin, Confinement Enhances the Diversity of Microbial Flow Fields, *Physical Review Letters* **123**, 248102 (2019).
- [39] D. Mondal, A. G. Prabhune, S. Ramaswamy, and P. Sharma, Strong confinement of active microalgae leads to inversion of vortex flow and enhanced mixing, *eLife* **10**, e67663 (2021).

- [40] C. Jin, Y. Chen, C. C. Maass, and A. J. T. M. Mathijssen, Collective Entrainment and Confinement Amplify Transport by Schooling Microswimmers, [Physical Review Letters](#) **127**, 088006 (2021).
- [41] H. C. Brinkman, A calculation of the viscosity and the sedimentation constant for solutions of large chain molecules taking into account the hampered flow of the solvent through these molecules, [Physica](#) **13**, 447 (1947).
- [42] R.-Y. Tsay and S. Weinbaum, Viscous flow in a channel with periodic cross-bridging fibres: Exact solutions and Brinkman approximation, [Journal of Fluid Mechanics](#) **226**, 125 (1991).
- [43] R. E. Pepper, M. Roper, S. Ryu, P. Matsudaira, and H. A. Stone, Nearby boundaries create eddies near microscopic filter feeders, [Journal of the Royal Society Interface](#) **7**, 851 (2010).
- [44] F. Gallaire, P. Meliga, P. Laure, and C. N. Baroud, Marangoni induced force on a drop in a Hele Shaw cell, [Physics of Fluids](#) **26**, 062105 (2014).
- [45] S. Whitaker, Flow in porous media I: A theoretical derivation of Darcy's law, [Transport in Porous Media](#) **1**, 3 (1986).
- [46] H. Nganguia and O. S. Pak, Squirming motion in a Brinkman medium, [Journal of Fluid Mechanics](#) **855**, 554 (2018).
- [47] C. de Blois, M. Reyssat, S. Michelin, and O. Dauchot, Flow field around a confined active droplet, [Physical Review Fluids](#) **4**, 054001 (2019).
- [48] W. Gilpin, V. N. Prakash, and M. Prakash, Flowtrace: Simple visualization of coherent structures in biological fluid flows, [Journal of Experimental Biology](#) **220**, 3411 (2017).
- [49] M. Morozov and S. Michelin, Nonlinear dynamics of a chemically-active drop: From steady to chaotic self-propulsion, [The Journal of Chemical Physics](#) **150**, 044110 (2019).
- [50] T. Ishikawa, M. P. Simmonds, and T. J. Pedley, Hydrodynamic interaction of two swimming model micro-organisms, [Journal of Fluid Mechanics](#) **568**, 119 (2006).
- [51] M. T. Downton and H. Stark, Simulation of a model microswimmer, [Journal of Physics: Condensed Matter](#) **21**, 204101 (2009).
- [52] N. Desai and S. Michelin, Instability and self-propulsion of active droplets along a wall, [Physical Review Fluids](#) **6**, 114103 (2021).
- [53] T. H. Tan, A. Mietke, J. Li, Y. Chen, H. Higinbotham, P. J. Foster, S. Gokhale, J. Dunkel, and N. Fakhri, Odd dynamics of living chiral crystals, [Nature](#) **607**, 287 (2022).

- [54] A. J. T. M. Mathijssen, F. Guzmán-Lastra, A. Kaiser, and H. Löwen, Nutrient Transport Driven by Microbial Active Carpets, [Physical Review Letters](#) **121**, 248101 (2018).
- [55] F. Guzmán-Lastra, H. Löwen, and A. J. T. M. Mathijssen, Active carpets drive non-equilibrium diffusion and enhanced molecular fluxes, [Nature Communications](#) **12**, 1906 (2021).
- [56] C. de Blois, V. Bertin, S. Suda, M. Ichikawa, M. Reyssat, and O. Dauchot, Swimming droplets in 1D geometries: An active Bretherton problem, [Soft Matter](#) **17**, 6646 (2021).

VI. SUPPLEMENTARY MATERIAL

A. Supplementary video captions

Movie S1: Flowtrace videos under bright-field microscopy corresponding to three vortex patterns in Fig.2, with $a = 61 \mu\text{m}$, $a = 80 \mu\text{m}$, and $a = 102 \mu\text{m}$ (left to right). The vortices around a pinned pumping droplet shift from the posterior to the anterior with increasing droplet diameter. Video clips are played in real time at 40fps and repeated multiple times for ease of viewing.

Movie S2: Flowtrace videos under bright-field microscopy corresponding to three vortex patterns in Fig.2, with $a = 148 \mu\text{m}$, $a = 185 \mu\text{m}$, and $a = 243 \mu\text{m}$ (left to right). The vortices around a pinned pumping droplet are multistable, showing, with increasing size, symmetric quadrupolar, strongly asymmetric dipolar, and, for the largest droplet, asymmetric quadrupolar patterns. Video clips are played in real time at 40fps and repeated multiple times for ease of viewing. Note that in the first panel, the oil droplet contained traces of $1 \mu\text{m}$ diameter colloidal silica particles leading to serendipitous visualisation of droplet internal flow field as well.

Movie S3: Dual-channel videomicroscopy underlying the data in Fig. 6 (the interface of a droplet being gradually saturated by chemical buildup). Black/white frame and green channel track colloidal tracers (Flowtrace), the red channel the fluorescent emission from oil filled micelles with Nile Red marker. The droplet itself is masked in black. Time in experiment displayed in minutes.

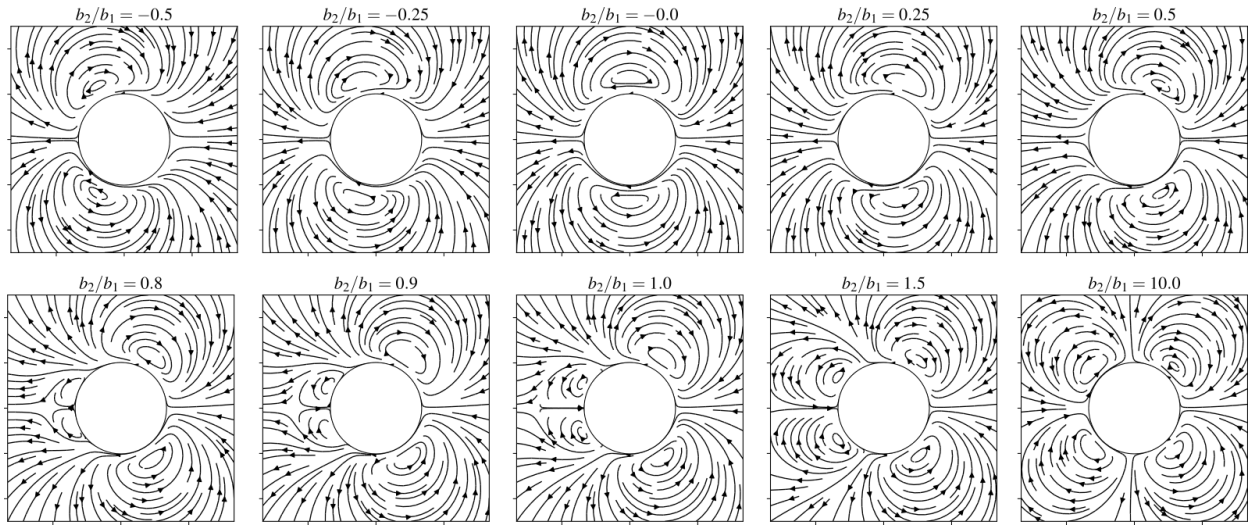


FIG. 8. Pumping flow field around a 2D Brinkman squirmer for increasing ratio of the squirmer parameter b_2/b_1 .